Signal-to-noise ratio comparison of angular signal radiography and phase stepping method*

Wali Faiz[1], Peiping Zhu(朱佩平)[2,†], Renfang Hu(胡仁芳)[3], Kun Gao(高昆)[1], Zhao Wu(吴朝)[1,‡], Yuan Bao(鲍园)[3], and Yangchao Tian(田扬超)[1,§]

[1] *National Synchrotron Radiation Laboratory, University of Science and Technology of China, Hefei* 230029, *China*
[2] *Institute of High Energy Physics, Chinese Academy of Sciences, Beijing* 100049, *China*
[3] *Shanghai United Imaging Healthcare Co. Ltd., Shanghai* 201807, *China*

(Received 13 June 2017; revised manuscript received 28 August 2017; published online 20 October 2017)

Grating-based x-ray phase contrast imaging has the potential to be applied in future medical applications as it is compatible with both laboratory and synchrotron source. However, information retrieval methods are important because acquisition speed, scanning mode, image quality, and radiation dose depend on them. Phase-stepping (PS) is a widely used method to retrieve information, while angular signal radiography (ASR) is a newly established method. In this manuscript, signal-to-noise ratios (SNRs) of ASR are compared with that of PS. Numerical experiments are performed to validate theoretical results. SNRs comparison shows that for refraction and scattering images ASR has higher SNR than PS method, while for absorption image both methods have same SNR. Therefore, our conclusions would have guideline in future preclinical and clinical applications.

Keywords: angular signal radiography (ASR), phase- stepping (PS), signal-to-noise ratio (SNRs), information retrieval method

PACS: 06.30.Bp, 42.30.Rx, 05.40.Ca, 42.25.Fx **DOI:** 10.1088/1674-1056/26/12/120601

1. Introduction

Conventional x-ray imaging has been widely used for non-destructive testing, security screening and biomedical imaging. Nonetheless, for low Z (atomic number) elements like biological soft tissues its image contrast is poor. X-ray phase-sensitive imaging techniques have potential to overcome contrast restriction. In the hard x-ray regime for low Z elements δ (real part decrement of the refractive index, associated with x-ray phase shift) is larger by about three orders of magnitude than β (imaginary part of refractive index, related with x-ray attenuation).[1] Moreover, Z dependency is lower for δ than β.[2] These facts indicate that x-ray phase-sensitive imaging techniques have potential of increased contrast for low Z elements.[3–5]

In the past two decades a number of x-ray phase-contrast imaging techniques have been developed.[6–13] Based on the signal retrieval, these methods are categorized into three types: the direct phase, the first derivative of phase (the differential phase), and the second derivative of phase of the object. Among these differential phases, the contrast imaging has divergent configurations like diffraction-enhanced imaging (DEI),[6,14] grating-based interferometric imaging,[8,10] grating-based non-interferometric imaging,[13] edge illumination.[11,12] Though, their configurations are different but they share some common characteristics.[15] The performance of all differential phase-contrast imaging can be depicted by rocking curve in DEI,[16] phase-stepping curve or shifting curve (SC) in grating-based imaging[8,17–19] and illumination curve in edge illumination[20] imaging. According to angular signal radiography (ASR) point of view rocking curve, phase stepping curve, and illumination curve are all angular signal response functions in the differential phase-contrast imaging.[16,21]

Specifically, grating-based x-ray phase-contrast imaging (GB-XPCI) has potential applications due to its compatibility with laboratory x-ray source along with synchrotron source and having large field of view (FOV).[8,22] Hence, clinical applications with GB-XPCI remain attainable. Beside attenuation and phase-contrast GB-XPCI is sensitive to scattering information which is linked with micron and sub-micron structural information of the object.[23] In GB-XPCI various information extraction methods: like phase-stepping (PS),[18] reverse projection (RP),[24] interlaced PS,[25] sliding window PS,[26] and ASR[21] have been developed to extract and sepa-

*Project supported by the National Research and Development Project for Key Scientific Instruments (Grant No. CZBZDYZ20140002), the National Natural Science Foundation of China (Grant Nos. 11535015, 11305173, and 11375225), the project supported by Institute of High Energy Physics, Chinese Academy of Sciences (Grant No. Y4545320Y2), and the Fundamental Research Funds for the Central Universities (Grant No. WK2310000065). The author, Wali Faiz, acknowledges and wishes to thank the Chinese Academy of Sciences and The World Academy of Sciences (CAS-TWAS) President's Fellowship Program for generous financial support.

†Corresponding author. E-mail: zhupp@ihep.ac.cn
‡Corresponding author. E-mail: wuzhao@ustc.edu.cn
§Corresponding author. E-mail: ychtian@ustc.edu.cn

© 2017 Chinese Physical Society and IOP Publishing Ltd

rate absorption, refraction and scattering signals. Among these methods, PS is one of the most extensively used information extraction methods. However, discontinuous image acquisition hinders its wide use in practical applications. On the other hand, interlaced PS and sliding window PS methods demand high angular sampling frequency for complex structure. Further, RP method is unable to extract scattering signal. In addition, ASR is a newly developed extraction method and has simplified phase retrieval algorithm and high image acquisition speed with reduced radiation dose.

First, the principles of ASR and PS will be reviewed briefly. In this article, noise properties of ASR and PS employing grating interferometer due to photon statistics using error propagation formula are discussed. The signal-to-noise ratios (SNRs) of the absorption, refraction and scattering images of the two methods show how system and sample parameters affect the noise behavior of GB-XPCI. This comparison is of great importance in future pre-clinical and clinical applications of GB-XPCI.

2. Background

GB-XPCI setup, as shown in Fig. 1(a), mainly consists of an x-ray source, splitter grating G1 (phase grating), analyzer grating G2 (absorption grating), and image detector. G1 having period p_1 causes a constant phase shift (generally $\pi/2$ or π) on incident x-rays. Due to fractional Talbot effect self-image pattern is formed downstream of G1.[17] However, the period of self-image is too small (about several micrometers) to be directly detected by the image detector. Hence, another grating G2 (having the same periodicity of self-imaging, p_2) is used to examine the intensity pattern. When one of the gratings is scanned along the direction orthogonal to its groove SC,[24] as a function of position in each detector pixel is obtained and shown in Fig. 1(b).

2.1. Angular signal radiography

In ASR, classical imaging description is applied to GB-XPCI system. ASR mainly deals with angle modulated function (AMF) connected with an object's physical properties like absorption, refraction, and scattering and angular signal response function (ASRF) determines sensitivity of GB-XPCI setup.[21] The incoming x-ray beam interacts via absorption, refraction, and scattering with the object. These interactions are summed up by AMF and are given as:

$$f(\psi;x,y) = I_0 \frac{\exp[-M(x,y)]}{\sqrt{2\pi}\vartheta_s(x,y)} \exp\left[-\frac{1}{2}\frac{\{\psi-\theta(x,y)\}^2}{\vartheta_s^2(x,y)}\right], \quad (1)$$

where $M(x,y)$ is absorption, $\theta(x,y)$ is refraction angle, $\vartheta_s^2(x,y)$ is scattering variance of sample, I_0 is incident photon number, and ψ is x-ray deviation angle.

In x-ray grating interferometer (XGI), by shifting the G2 perpendicular to both grating lines and the incident beam without object, ASRF can be measured with detector, e.g., $S(\psi) = S(x_g/d)$ and can be fitted with cosine function.[4,5] Further, when scanning steps are more then SC will be more accurate. In ASR, data are investigated on four typical positions (valley V, up-slope U, peak P, and down-slope D, shown in Fig. 1(b)) on the SC and are given as:

$$S(\psi) = \overline{S}\left[1 - V_0 \cos\left(\frac{2\pi d}{p_2}(\psi+\psi_0) + \eta\frac{\pi}{2}\right)\right], \quad (2)$$

where $\overline{S} = (S_{\max}+S_{\min})/2$ is the mean value, $V_0 = (S_{\max}-S_{\min})/(S_{\max}+S_{\min})$ is visibility, $S_{\max}$ is maximum, $S_{\min}$ is minimum value of SC, d is the inter-grating distance, ψ_0 is initial deviation angle, and $\eta = 0,1,2,3$ is modulation parameter.

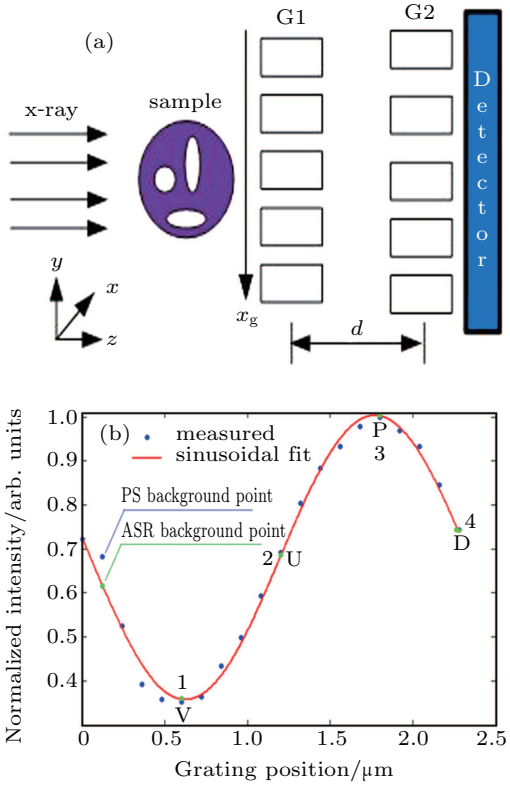


Fig. 1. (color online) (a) Schematic setup of GB-XPCI (b) exemplary shifting curve.

Based on ASR in XGI, the four sample imaging equations can be depicted as:

$$\begin{aligned} I^s(x,y) &= f(\psi;x,y) \otimes S(\psi) \\ &= I_0\overline{S}\mathrm{e}^{-M(x,y)}\left[1 - V_0\,\mathrm{e}^{-2\pi^2 d^2 \vartheta_s^2(x,y)/p_2^2}\right. \\ &\quad \left.\times \cos\left(\frac{2\pi d}{p_2}(\theta(x,y)+\psi_0) + \eta\frac{\pi}{2}\right)\right], \end{aligned} \quad (3)$$

where $\otimes$ stands for convolution. The four typical imaging equations can be obtained by $\eta = 0,1,2,3$.

In order to eliminate ψ_0, generally caused by local imperfection of the grating, projection images with and without sample are taken and then effective absorption, refraction, and

scattering information of the sample are extracted as (for simplicity here we drop (x,y)):

$$M = \ln\left[\frac{I_{\rm U}^{\rm b}+I_{\rm D}^{\rm b}+I_{\rm V}^{\rm b}+I_{\rm P}^{\rm b}}{I_{\rm U}^{\rm s}+I_{\rm D}^{\rm s}+I_{\rm V}^{\rm s}+I_{\rm P}^{\rm s}}\right], \tag{4}$$

$$\theta = -\frac{p_2}{2\pi d}\left[\arctan\left(\frac{I_{\rm U}^{\rm s}-I_{\rm D}^{\rm s}}{I_{\rm V}^{\rm s}-I_{\rm P}^{\rm s}}\right) - \arctan\left(\frac{I_{\rm U}^{\rm b}-I_{\rm D}^{\rm b}}{I_{\rm V}^{\rm b}-I_{\rm P}^{\rm b}}\right)\right], \tag{5}$$

$$\vartheta_s^2 = -\frac{p_2^2}{2\pi^2 d^2}\left\{\ln\left[\frac{\sqrt{\left(I_{\rm U}^{\rm s}-I_{\rm D}^{\rm s}\right)^2+\left(I_{\rm V}^{\rm s}-I_{\rm P}^{\rm s}\right)^2}}{V_0\left(I_{\rm U}^{\rm s}+I_{\rm D}^{\rm s}\right)}\right] - \ln\left[\frac{\sqrt{\left(I_{\rm U}^{\rm b}-I_{\rm D}^{\rm b}\right)^2+\left(I_{\rm V}^{\rm b}-I_{\rm P}^{\rm b}\right)^2}}{V_0\left(I_{\rm U}^{\rm b}+I_{\rm D}^{\rm b}\right)}\right]\right\}, \tag{6}$$

where $I_{\rm V}^{\rm b}, I_{\rm U}^{\rm b}, I_{\rm P}^{\rm b}, I_{\rm D}^{\rm b}$ and $I_{\rm V}^{\rm s}, I_{\rm U}^{\rm s}, I_{\rm P}^{\rm s}, I_{\rm D}^{\rm s}$ are background and sample images at position valley, up-slope, peak, and down-slope respectively.

2.2. Phase stepping method

In the case of PS method one of the gratings is uniformly scanned for phase steps $J(J \geq 3)$ within one period. The photon number detected by detector at each pixel is given by Fourier series expansion.

$$I_j(x,y) = a_0 + a_1\cos\left(\frac{2\pi d}{p_2}\left(\theta\left(x,y\right)\right) + 2\pi\frac{j}{J} + \psi_0\right), \quad j = 1,2,3,\ldots,J, \tag{7}$$

where a_0 and a_1 are Fourier coefficient.

When a sample is put in the x-ray beam path, it absorbs, refracts, and scatters x-rays. Using 4-step PS, the absorption, refraction and scattering of the sample can be extracted as[18]

$$M = \ln\left[\frac{I_1^{\rm b}+I_2^{\rm b}+I_3^{\rm b}+I_4^{\rm b}}{I_1^{\rm s}+I_2^{\rm s}+I_3^{\rm s}+I_4^{\rm s}}\right], \tag{8}$$

$$\theta = -\frac{p_2}{2\pi d}\left[\arctan\left(\frac{I_2^{\rm s}-I_4^{\rm s}}{I_1^{\rm s}-I_3^{\rm s}}\right) - \arctan\left(\frac{I_2^{\rm b}-I_4^{\rm b}}{I_1^{\rm b}-I_3^{\rm b}}\right)\right], \tag{9}$$

$$\vartheta_s^2 = \frac{p_2^2}{2\pi^2 d^2}\ln\left[\frac{\sqrt{\left(I_2^{\rm b}-I_4^{\rm b}\right)^2+\left(I_1^{\rm b}-I_3^{\rm b}\right)^2}}{\left(I_2^{\rm b}+I_4^{\rm b}\right)} \times \frac{\left(I_2^{\rm s}+I_4^{\rm s}\right)}{\sqrt{\left(I_2^{\rm s}-I_4^{\rm s}\right)^2+\left(I_1^{\rm s}-I_3^{\rm s}\right)^2}}\right], \tag{10}$$

where $I_1^{\rm b}, I_2^{\rm b}, I_3^{\rm b}, I_4^{\rm b}$ and $I_1^{\rm s}, I_2^{\rm s}, I_3^{\rm s}, I_4^{\rm s}$ are background and sample images at positions 1, 2, 3, 4 (shown in Fig. 1(b)) respectively.

3. Theory: Noise properties

Photon statistical noise, being one of the major causes of noise in GB-XPCI is discussed in this section. In the retrieval process, photon noise of the projection images shifts uncertainties to the extracted absorption, refraction, and scattering signals. The uncertainties in all the three signals of ASR are calculated and compared with PS method,[28] with the help of error propagation formula,[29] and are given in Table 1.

Table 1. Expressions of the SNRs of ASR and PS for absorption, refraction and scattering images due to photon statistical noise (for simplicity (x,y) are omitted).

	ASR	PS
Absorption	$2\sqrt{I_0\overline{S}\,\mathrm{e}^{-M}\overline{M}}$	$2\sqrt{I_0'\overline{S'}\,\mathrm{e}^{-M}\overline{M}}$
Refraction	$\left(\frac{2\sqrt{2}\pi d}{p_2}\right)V\sqrt{I_0\overline{S}\,\mathrm{e}^{-M}\overline{\theta}}$	$\left(\frac{2\sqrt{2}\pi d}{p_2}\right)V'\sqrt{I_0'\overline{S'}\,\mathrm{e}^{-M}\overline{\theta}}$
Scattering	$\left(\frac{2\sqrt{2}\pi^2 d^2}{p_2^2}\right)\frac{V\sqrt{I_0\overline{S}\,\mathrm{e}^{-M}\overline{\vartheta_s^2}}}{\sqrt{1+V^2-2V^2\sin^2\left(\frac{2\pi d}{p_2}\theta\right)}}$	$\left(\frac{2\sqrt{2}\pi^2 d^2}{p_2^2}\right)\frac{V'\sqrt{I_0'\overline{S'}\,\mathrm{e}^{-M}\overline{\vartheta_s^2}}}{\sqrt{1+V'^2-2V'^2\sin^2\left(\frac{2\pi d}{p_2}\theta\right)}}$

From SNRs of ASR and PS for absorption, refraction, and scattering images (given in Table 1), we deduce the following six items:

(i) SNRs of both ASR and PS for all three images are directly proportional to the square root of the incident photon number.

(ii) SNRs of both ASR and PS for all three images depend upon absorption of the sample.

(iii) SNRs of both ASR and PS for all three images depend upon mean value of background SC of respective methods.

(iv) SNRs of absorption images of both ASR and PS methods are independent of the system parameters. On the other hand, SNRs of both ASR and PS for refraction images are proportional to inter-grating distance (d) and inversely proportional to period of analyzer grating (p_2). Meanwhile SNRs of ASR and PS for scattering images are proportional to square of the inter-grating distance and inversely proportional to square of the period of analyzer grating.

(v) SNRs of both ASR and PS for refraction and scatter-

ing images depend upon visibility of sample SC of respective methods.

(vi) SNRs of ASR and PS for scattering images depend upon the refraction angle.

Now taking the ratio of the standard deviations of ASR and PS:

$$R_M = \frac{\sigma_M^{\mathrm{ASR}}}{\sigma_M^{\mathrm{PS}}} = \sqrt{\frac{I_0'\overline{S'}}{I_0\overline{S}}}, \tag{11}$$

$$R_\theta = \frac{\sigma_\theta^{\mathrm{ASR}}}{\sigma_\theta^{\mathrm{PS}}} = \sqrt{\frac{I_0'\overline{S'}}{I_0\overline{S}}}\left(\frac{V'}{V}\right), \tag{12}$$

$$R_{\vartheta_s^2} = \frac{\sigma_{\vartheta_s^2}^{\mathrm{ASR}}}{\sigma_{\vartheta_s^2}^{\mathrm{PS}}} = \sqrt{\frac{I_0'\overline{S'}}{I_0\overline{S}}}\left(\frac{V'}{V}\right)\frac{\sqrt{1+V^2-2V^2\sin^2\left(\frac{2\pi d}{p_2}\theta\right)}}{\sqrt{1+V'^2-2V'^2\sin^2\left(\frac{2\pi d}{p_2}\theta\right)}}, \tag{13}$$

where

$$V(x,y) = V_0\exp\left[\frac{-2\pi^2d^2\vartheta_s^2(x,y)}{p_2^2}\right],$$

$$V'(x,y) = V_0'\exp\left[\frac{-2\pi^2d^2\vartheta_s^2(x,y)}{p_2^2}\right].$$

Equations (11)–(13) show ratio of standard deviations of ASR and PS method for absorption, refraction, and scattering images. Here, we have used four steps for both ASR and PS, so the incident photon number in both methods is the same ($I_0 = I_0'$). The ratio of the standard deviation of ASR and PS for absorption images depends upon mean values of the background SC while for refraction and scattering images depend upon visibility of the corresponding methods. In ASR, many steps are used to get the background SC, after that the background SC is fitted with cosine curve. In other words, in ASR the ASRF is more accurate than SC of the PS method.

4. Simulation and discussion

To validate theoretical derivations, numerical simulations using Matlab, based on ray optical approach are performed. The pitches of phase and absorption grating of Talbot interferometer are the same $p_1 = p_2 = 4$ μm. The interferometer is operated by a monochromatic x-ray beam of energy 25 keV. The inter-grating distance was set to first fractional Talbot distance of 16.13 cm. The cylinder of polymethyl methacrylate (PMMA) with a radius of 5 mm is used as sample. The refractive index of the sample is $n = 1 - 4.22\times10^{-7} + \mathrm{i}1.81\times10^{-10}$ at 25 keV. Four sample images are taken to extract absorption, refraction and scattering information in both ASR and PS methods. The SNRs of ASR and PS are compared for various incident photon intensities. In both ASR and PS methods the same total photon number is used.

Figures 2(a) and 2(b) show calculated absorption images of ASR and PS methods respectively. Figure 2(c) shows the SNRs comparison of the corresponding absorption images of the four-step ASR and PS. In both methods excellent agreement is achieved between simulation and theoretical derivations, which validates theoretical model. Under the same total exposure, the SNRs of ASR and PS methods for absorption image are compared. The SNRs of both methods are compared versus incident photon number and shown in Fig. 2(c). The comparison shows that SNR of ASR for absorption image is closely the same as SNR of the PS method.

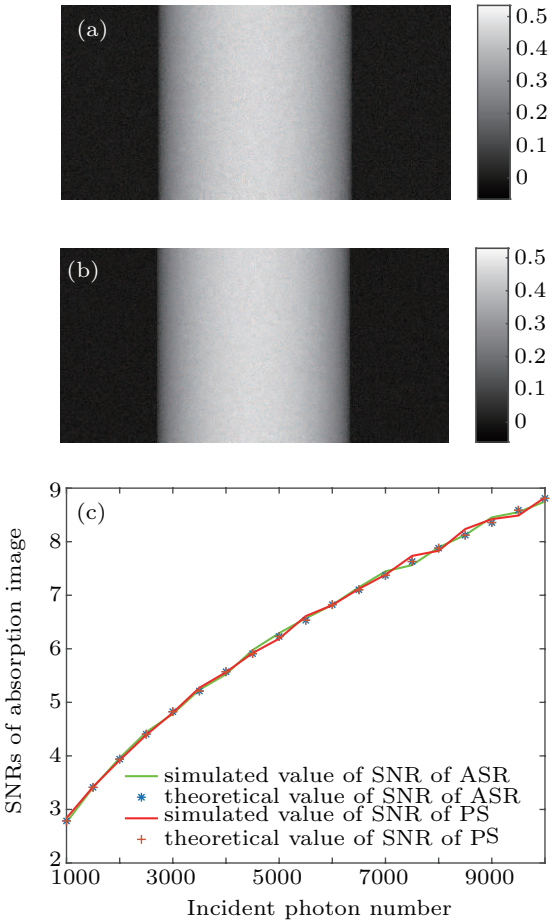


Fig. 2. (color online) Calculated absorption images of (a) ASR, (b) PS, and (c) signal-to-noise ratio comparison of four steps ASR and PS for absorption image.

The calculated refraction images of ASR and PS are shown in Figs. 3(a) and 3(b). In Fig. 3(c) the comparison of SNRs of refraction images of ASR and PS are shown. In both methods simulation and theoretical results match well, which validates our theoretical model. The SNRs of ASR and PS methods for refraction images are compared under the same input parameters. Figure 3(c) shows the relationship of SNRs of ASR and PS of refraction image and incident photon number. It can be seen in Fig. 3(c) that SNRs of ASR for refraction images are higher than SNRs of the PS method. Figures 4(a) and 4(b) represent scattering images obtained by ASR and PS respectively and the corresponding SNRs are shown in

Fig. 4(c). It is clear from Fig. 4(c) that theoretical results are in good agreement with simulation results, hence validating our theoretical model. The SNRs of ASR and PS methods as a function of incident photon number for scattering images are shown in Fig. 4(c), which are obtained when input parameters are kept identical. The comparison shows that scattering image of ASR has higher SNRs than scattering image of PS.

Here, we point out that in ASR, ASRF is obtained with a high number of steps after that take four typical images. In this way the dose delivered to the sample is low. In fact, this is useful for medical application, as a high dose is used to get ASRF and we use a low dose to get sample images. However in PS, the number of steps for background without sample is the same as that for images with sample. This is the reason that ASRF in ASR is more accurate than SC in PS, so high quality images can be obtained using ASR.

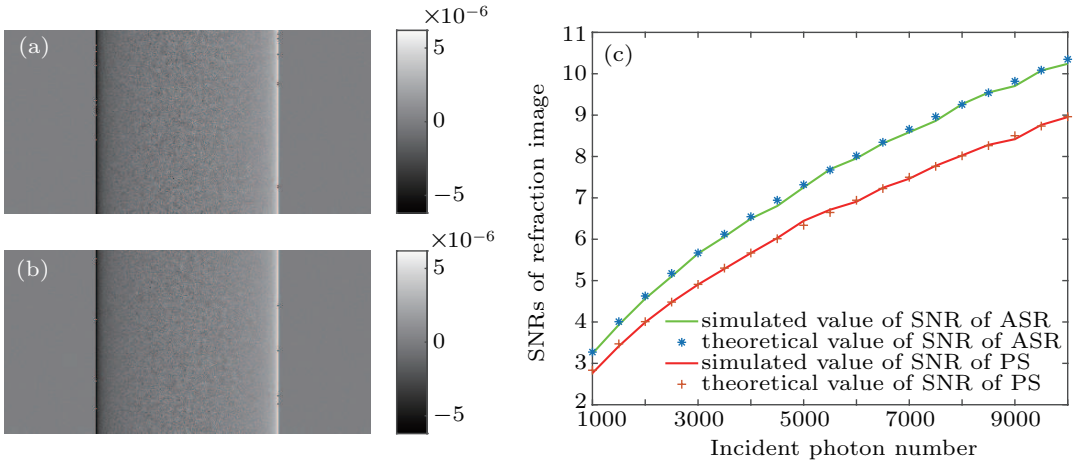


Fig. 3. (color online) Calculated refraction images of (a) ASR, (b) PS, and (c) signal-to-noise ratios of four steps ASR and PS for refraction image.

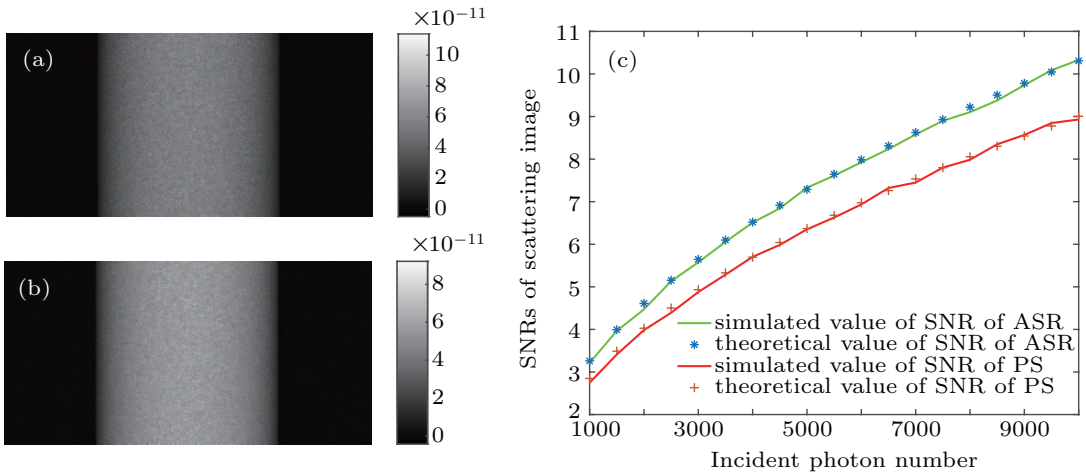


Fig. 4. (color online) Calculated scattering images of (a) ASR, (b) PS, and (c) signal-to-noise ratio comparison scattering images of four steps ASR and PS.

5. Conclusion

In this paper, theoretical analysis of noise properties retrieved by ASR for absorption, refraction, and scattering images in grating-based x-ray phase-contrast imaging is presented and compared with PS method. Theoretical derivations are validated by computer simulations. In addition, ratios of standard deviations of both methods for absorption, refraction, and scattering images are discussed. Furthermore, SNRs of ASR and PS methods are compared. The comparison shows that ASR has higher SNR for refraction and scattering images, while both methods have nearly the same SNR for absorption image.

References

[1] Momose A and Fukuda J 1995 *Med. Phys.* **22** 375
[2] Als-Nielsen J and Mcmorrow D 2001 *Elements of Modern X-Ray Physics*, ISBN: 0-471-49857-2
[3] Fitzgerald R 2000 *Phys. Today* **53** 23
[4] Momose A 2003 *Opt. Express* **11** 2303
[5] Momose A 2005 *Jpn. J. Appl. Phys.* **44** 6355
[6] Chapman D, Thomlinson W, Johnston R E, Washburn D, Pisano E, Gmur N, Zhong Z, Menk R, Arfelli F and Sayers D 1997 *Phys. Med. Biol.* **42** 2015
[7] Zhu P P, Yuan Q X, Huang W X, Wang J Y, Shu H, Chen B, Liu Y J, Li E and Wu Z Y 2006 *J. Phys. D: Appl. Phys.* **39** 4142
[8] Pfeiffer F, Weitkamp T, Bunk O and David C 2006 *Nat. Phys.* **2** 258
[9] Wen H H, Bennett E E, Kopace R 2010 *Opt. Express* **35** 1932
[10] Wang Z, Gao K, Wang D 2014 *Opt. Lett.* **39** 877
[11] Hagen C K, Diemoz P C, Endrizzi M 2014 *Opt. Express* **22** 7989

[12] Olivo A, Diemoz P C, Bravin A 2012 *Opt. Lett.* **37** 915
[13] Huang Z F, Kang K J, Zhang L 2009 *Phys. Rev. A* **79**
[14] Zhu P P, Yuan Q X, Huang W X, Wang J Y, Shu H, Chen B, Liu Y J, Li E and Wu Z Y 2006 *J. Phys. D: Appl. Phys.* **39** 4142
[15] Zhu P P, Zhu Z Z, Hong Y L, Zhang K, Huang W X, Yuan Q X, Zhao X J, Ju Z Q, Wu Z Y, Wei Z, Wiebe S and Chapman L D 2014 *Appl. Opt.* **53** 861
[16] Bao Y, Wang Y, Li P 2015 *J. Syn. Rad.* **22** 786
[17] Momose A, Kawamoto S, Koyama I, Hamaishi Y, Takai K and Suzuki Y 2003 *Jpn. J. Appl. Phys.* **42** L866
[18] Weitkamp T, Diaz A, David C, Pfeiffer F, Stampanoni M, Cloetens P and Ziegler E 2005 *Opt. Express* **13** 6296
[19] Momose A, Yashiro W, Takeda Y 2006 *Jpn. J. Appl. Phys.* **45** 5254
[20] Zamir A, Endrizzi M and Hagen C K 2016 *Sci. Rep.* **6** 31197
[21] Li P, Zhang K, Bao Y, Ren Y Q, Ju Z Q, Wang Y, He Q L, Zhu Z Z, Huang W X, Yuan Q X and Zhu P P 2016 *Opt. Express* **24** 5829
[22] Pfeiffer F, Kottler C, Bunk O 2007 *Phys. Rev. Lett.* **98** 108105
[23] Pfeiffer F, Bech M, Bunk O, Kraft P, Eikenberry E F, Bronnimann C H, Grunzweig C and David C 2008 *Nat. Mater.* **7** 134
[24] Zhu P P, Zhang K, Wang Z L, Liu Y J, Liu X S, Wu Z Y, Mcdonald S A, Marone F and Stampanoni M 2010 *Proc. Natl. Acad. Sci. USA* **107** 13576
[25] Zanette I, Bech M, Pfeiffer F and Weitkamp T 2011 *Appl. Phys. Lett.* **98** 094101
[26] Zanette I, Bech M, Rack A, Duc G L, Tafforeau P, David C, Mohr J, Pfeiffer F and Weitkamp T 2012 *Proc. Natl. Acad. Sci. USA* **109** 10199
[27] Diemoz P, Coan P, Zanette I 2011 *Opt. Express* **19** 1691
[28] Revol V, Kottler C, Kaufmann R, Straumann U and Urban C 2010 *Rev. Sci. Instrum.* **81** 073709
[29] Bronshtein I N, Semendyayev K A, Musiol G and Muehlig H 2013 *Handbook of Mathematics New York Springer Science & Business Media*